LETTER

Temporal and spectral fingerprints of ultrafast all–coherent spin switching

S. Schlauderer[1,9], C. Lange[1,9]*, S. Baierl[1], T. Ebnet[1], C. P. Schmid[1], D. C. Valovcin[2], A. K. Zvezdin[3,4,5], A. V. Kimel[6,7], R. V. Mikhaylovskiy[7,8]* & R. Huber[1]

Future information technology demands ever-faster, low-loss quantum control. Intense light fields have facilitated milestones along this way, including the induction of novel states of matter[1–3], ballistic acceleration of electrons[4–7] and coherent flipping of the valley pseudospin[8]. These dynamics leave unique 'fingerprints', such as characteristic bandgaps or high-order harmonic radiation. The fastest and least dissipative way of switching the technologically most important quantum attribute—the spin—between two states separated by a potential barrier is to trigger an all-coherent precession. Experimental and theoretical studies with picosecond electric and magnetic fields have suggested this possibility[9–11], yet observing the actual spin dynamics has remained out of reach. Here we show that terahertz electromagnetic pulses allow coherent steering of spins over a potential barrier, and we report the corresponding temporal and spectral fingerprints. This goal is achieved by coupling spins in antiferromagnetic $TmFeO_3$ (thulium orthoferrite) with the locally enhanced terahertz electric field of custom-tailored antennas. Within their duration of one picosecond, the intense terahertz pulses abruptly change the magnetic anisotropy and trigger a large-amplitude ballistic spin motion. A characteristic phase flip, an asymmetric splitting of the collective spin resonance and a long-lived offset of the Faraday signal are hallmarks of coherent spin switching into adjacent potential minima, in agreement with numerical simulations. The switchable states can be selected by an external magnetic bias. The low dissipation and the antenna's subwavelength spatial definition could facilitate scalable spin devices operating at terahertz rates.

The lowest theoretical limit on energy dissipation when manipulating one bit of information is defined by the Landauer principle[12] as $Q = k_B T \ln 2$, where T is the temperature and k_B denotes the Boltzmann constant. This can be seen as a result of the inelastic scattering of a quasiparticle of energy Q, such as a collective spin excitation, called a magnon. At or below room temperature, Q is of the order of millielectronvolt, which by the uncertainty principle entails picosecond timescales for minimally dissipative switching. Thus, precessional switching[9,10,13,14] triggered by a single-cycle terahertz (THz) pulse with millielectronvolt photon energies and subpicosecond duration promises the fastest and least-dissipative magnetic control.

Experimentally, ultrafast spin control has come a long way[15–17] from the discovery of subpicosecond laser-induced spin dynamics[18] to all-optical non-thermal recording[19]. Understanding strongly non-equilibrium spin dynamics triggered by THz pulses, however, is still in its infancy. In antiferromagnets, magnons feature resonance energies in the millielectronvolt range[20] and can be directly addressed by the magnetic field component of intense THz pulses[21–23]. Because the underlying Zeeman interaction is relatively weak, magnetic field amplitudes that allow a complete spin reversal have only been reached in linear accelerators[9], where the spin dynamics have not been accessible on the

intrinsic femtosecond scale. Also, spin-transfer torques mediated by THz-driven electric currents have induced switching of antiferromagnetic domains, yet without ultrafast temporal resolution[24].

Conversely, electromagnons and the more universal coupling of crystal-field-split electronic transitions or coherent phonons with the magnetic anisotropy field have allowed the electric THz field component to drive large-amplitude magnons, observed directly in the time domain[22,25,26]. The available THz peak electric field of 1 MV cm^{-1} has, however, limited the maximum spin excursion far below critical values needed for a complete spin reversal. Meanwhile, the near-field enhancement in custom-tailored antenna structures has been exploited to sculpt atomically strong THz waveforms, sufficient to drive non-perturbative
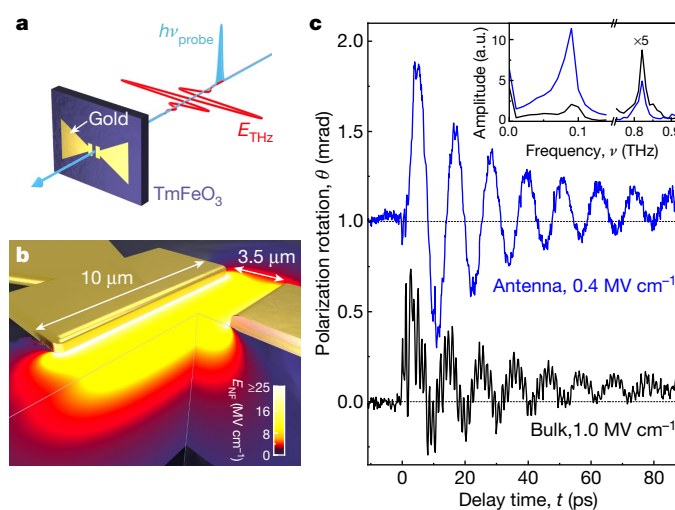
Fig. 1 | Antenna-enhanced THz spin dynamics. a, Schematic of the gold bowtie antenna on $TmFeO_3$. The structure is excited from the back side by an intense THz electric field E_{THz} (red waveform) while a co-propagating near-infrared pulse ($h\nu_{probe}$; light blue) probes the induced magnetization dynamics in the feed gap between the two lobes of the antenna. **b**, Peak near-field amplitude, E_{NF} (see colour scale at bottom right), in the antenna feed gap calculated by finite-difference simulations for a real incident THz waveform with a peak field amplitude of $E_{THz} = 1.0$ MV cm^{-1} (see Extended Data Fig. 1c). **c**, Experimentally detected polarization rotation signal as a function of the delay time, t, obtained for a peak electric THz field of $E_{THz} = 1.0$ MV cm^{-1} on the unstructured substrate (black curve), and when probing the feed gap of the bowtie antenna structure resonantly using a THz waveform with a peak electric far-field amplitude of $E_{THz} = 0.4$ MV cm^{-1} (blue curve; vertically offset by 1 mrad for better visibility). Inset, corresponding amplitude spectra featuring two modes (at 0.09 THz and 0.82 THz). The sample was kept at a lattice temperature of $T = 83$ K. a.u., arbitrary units.

[1]Department of Physics, University of Regensburg, Regensburg, Germany. [2]Department of Physics and the Institute for Terahertz Science and Technology, University of California at Santa Barbara, Santa Barbara, CA, USA. [3]Prokhorov General Physics Institute of the Russian Academy of Sciences, Moscow, Russia. [4]P.N. Lebedev Physical Institute of the Russian Academy of Sciences, Moscow, Russia. [5]Magnetic Heterostructures and Spintronics Laboratory, Moscow Institute of Physics and Technology (State University), Dolgoprudny, Russia. [6]Laboratory for Ultrafast Dynamics in Ferroics, Russian Technological University (MIREA), Moscow, Russia. [7]Institute for Molecules and Materials, Radboud University, Nijmegen, The Netherlands. [8]Present address: Department of Physics, Lancaster University, Bailrigg, UK. [9]These authors contributed equally: S. Schlauderer, C. Lange.. *e-mail: christoph.lange@ur.de; r.mikhaylovskiy@lancaster.ac.uk
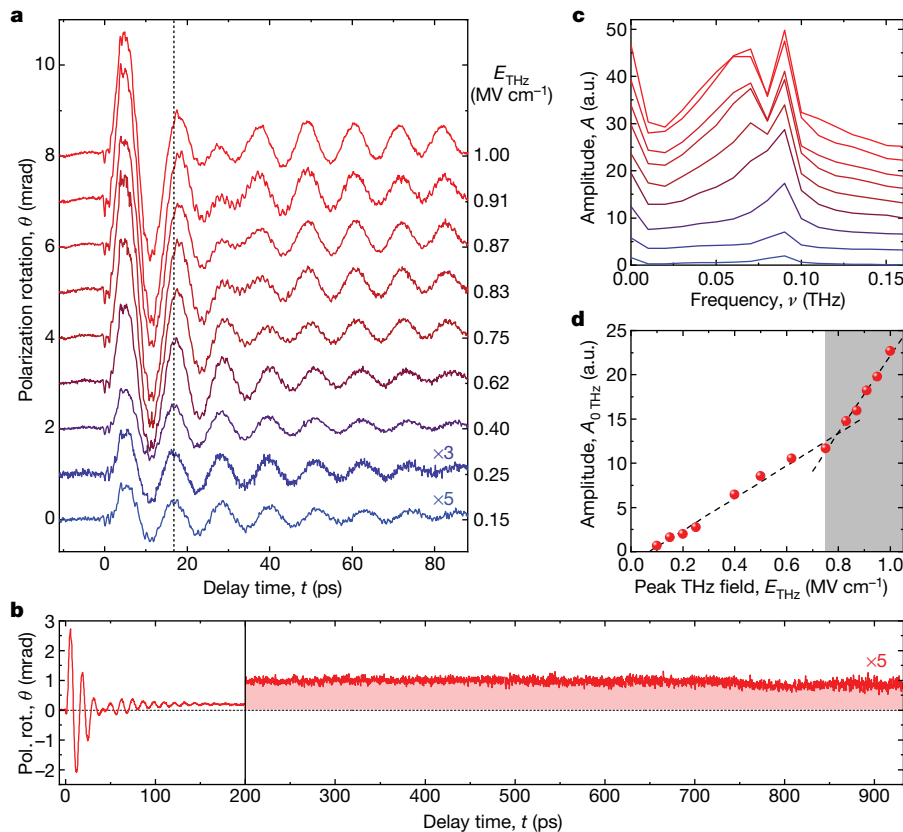
Fig. 2 | THz-induced nonlinear spin dynamics. a, Polarization rotation of the near-infrared probe pulse focussed through the centre of the antenna feed gap for various far-field amplitudes, as a function of the delay time, t. For incident THz peak fields $E_{THz} > 0.75$ MV cm^{-1} (labelled at right), the quasi-monochromatic oscillation is strongly distorted by a phase slip at delay times between 25 ps and 35 ps. The data are offset and scaled as indicated for clarity. Lattice temperature, $T = 83$ K. **b**, Long-term evolution of the polarization rotation (Pol. rot.) for a THz peak field of $E_{THz} = 1.0$ MV cm^{-1}. The red-shaded area indicates the long-lived offset; note the ×5 vertical magnification after $t = 200$ ps. **c**, Spectral amplitude of the time-domain data shown in **a**. The phase slip in the polarization rotation signal for the highest THz fields manifests itself in a splitting of the quasi-ferromagnetic resonance. **d**, Spectral amplitude of the d.c. offset, $A_{0\,THz}$, as a function of the THz far-field peak amplitude, E_{THz}. $A_{0\,THz}$ increases monotonically with the THz field. The grey-shaded area indicates the spin-switching regime with increased slope of $A_{0\,THz}$. Dashed lines are guides to the eye.

nonlinearities, such as THz-induced phase transitions[27] and interband Zener tunnelling, with subdiffractional spatial definition[28]. Such enhancement of the electric field has not yet been used for coherent spin control.

Here we combine the advantages of electric-field-induced anisotropy changes in an antiferromagnet with the local near-field enhancement of metal antennas. We ballistically steer spins over potential barriers to achieve THz-driven switching between stable states while observing these dynamics directly on the femtosecond scale. The experiments are performed in high-quality single crystals of the model antiferromagnet TmFeO$_3$. The antiferromagnetically ordered Fe^{3+} spins are slightly canted by the Dzyaloshinskii–Moriya interaction, resulting in a net ferromagnetic moment. As the magnetic anisotropy depends on temperature[26], the spins undergo reorientation phase transitions at $T_1 = 80$ K and $T_2 = 90$ K. The anisotropy may also be modified by THz electric dipole transitions between crystal-field-split states of the electronic ground state of the Tm^{3+} ions, the angular momenta of which are coupled with the Fe^{3+} spins by exchange and dipolar interactions[29]. Our idea is to abruptly change the magnetic anisotropy by sufficiently strong THz pulses, causing the spins to switch fully ballistically.

We fabricate custom-tailored bowtie antennas of gold (feed gap, 3.5 μm) on a 60-μm-thick single crystal of TmFeO$_3$ (Extended Data Fig. 1) to bypass the diffraction limit and maximize the achievable THz amplitude. The design was guided by numerical finite-difference frequency-domain simulations optimizing the near-field enhancement at a frequency of 0.65 THz (see Methods), which is resonant with crystal-field-split ground-state transitions in Tm^{3+}. In a pump–probe scheme

(Fig. 1a), an intense THz transient with tunable far-field amplitudes of up to $E_{THz} = 1.0$ MV cm^{-1} (see Methods) excites the structure from the TmFeO$_3$ back side. The ensuing spin dynamics are probed via the polarization rotation, θ, imprinted on a co-propagating femtosecond near-infrared pulse (wavelength, 807 nm; pulse duration, 33 fs) by the Faraday effect and magnetic linear dichroism. Our quantitative simulation shows that, for the strongest electro-optically detected THz waveform, the near field of the antenna, E_{NF}, readily exceeds 9 MV cm^{-1} in the centre of the gap (Fig. 1b).

To test the efficiency of the antenna, we compare the magneto-optical signal induced in TmFeO$_3$ in the transition phase ($T = 83$ K) with and without the near-field antenna, as a function of the pump–probe delay time, t. In the absence of an antenna, a THz pulse with an amplitude of $E_{THz} = 1.0$ MV cm^{-1} abruptly sets off coherent magnon oscillations, which decay exponentially within 40 ps (Fig. 1c, black curve). The signal consists of a superposition of two frequency components centred at 0.09 THz and 0.82 THz (Fig. 1c inset)—the quasi-ferromagnetic (q-fm) and the quasi-antiferromagnetic (q-afm) mode[26], respectively. The maximum rotation angle of the probe polarization of 0.5 mrad corresponds to a magnetization deflection by 3.5° (see Methods). By contrast, we observe a qualitatively different response when the probe pulse is positioned in the centre of the antenna feed gap. Here a polarization rotation as high as 0.9 mrad is reached for a much weaker THz far field of $E_{THz} = 0.4$ MV cm^{-1} (Fig. 1c, blue curve). In addition, the relative spectral amplitude of the q-fm mode is substantially enhanced, whereas the amplitude of the q-afm mode is suppressed. This behaviour is expected because the q-fm mode is excited by the antenna-enhanced
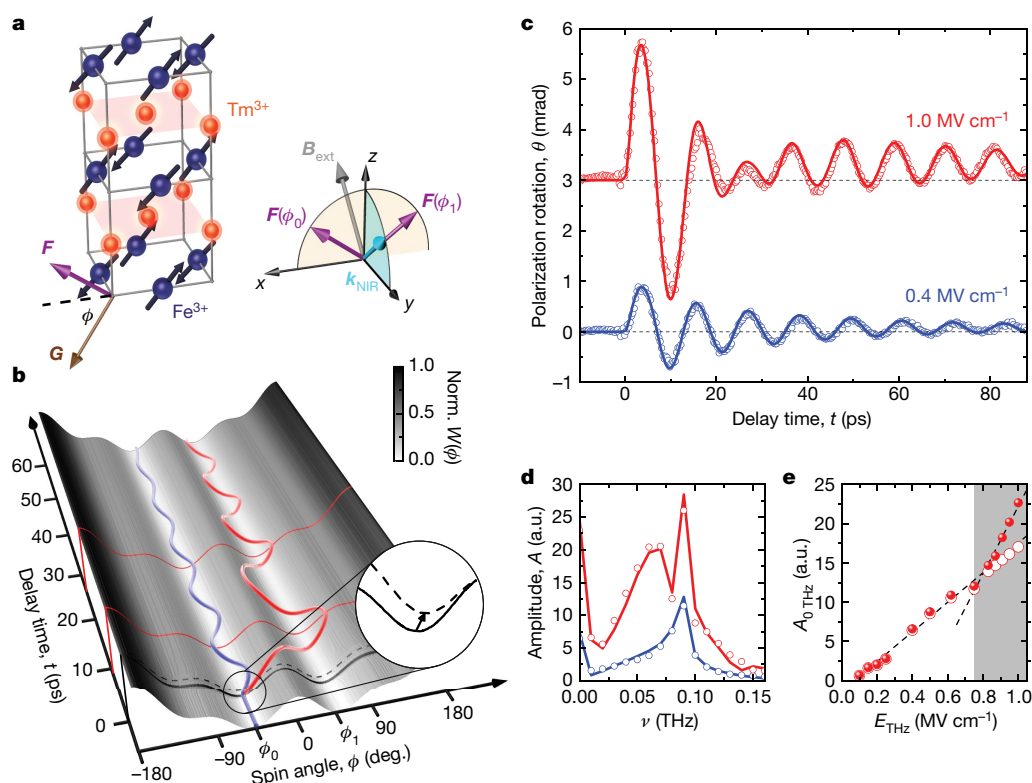
Fig. 3 | Microscopic picture of ballistic spin motion. a, Spin and lattice structure of TmFeO$_3$ in the Γ_{24} phase ($T_1 < T < T_2$), showing the Fe^{3+} spins (dark blue spheres and arrows), Tm^{3+} ions (orange spheres), and the ferromagnetic moment, $\boldsymbol{F}$ (violet arrow). The antiferromagnetic vector, $\boldsymbol{G}$ (brown arrow), lies in the x–z plane and encloses a finite angle of $0° < \phi < 90°$ with the x axis. Inset, geometry of the wave vector of the probe pulse, $\boldsymbol{k}_{\mathrm{NIR}}$ (light blue arrow), with respect to $\boldsymbol{F}$ and the external magnetic field $\boldsymbol{B}_{\mathrm{ext}}$ (grey arrow). **b**, Numerical simulation of THz-induced ballistic spin dynamics. On THz excitation, the magnetic potential $W(\phi)$ is abruptly modified near a delay time of $t = 0$ ps (shown magnified in the inset). Near-field THz transients with peak amplitudes of $E_{\mathrm{NF}} = 6$ MV cm^{-1} abruptly induce large-amplitude spin oscillations within the same potential valley around the initial angle ϕ_0 (blue trajectory). For a THz near field of $E_{\mathrm{NF}} = 10$ MV cm^{-1}, the spins reach the adjacent local minimum (red trajectory) at ϕ_1, where $\phi_1 \approx \phi_0 + 90°$, accumulating

a phase retardation relative to spins oscillating around ϕ_0 (delay times $t = 9.7$ ps and 27.2 ps, respectively; red cuts through the magnetic potential). **c**, Calculated polarization rotation in the antenna feed gap for an incident THz electric peak field amplitude of $E_{\mathrm{THz}} = 0.4$ MV cm^{-1} (blue curve) and $E_{\mathrm{THz}} = 1.0$ MV cm^{-1} (red curve) as a function of the delay time, t, for a lattice temperature of $T = 83$ K, normalized to the experimental peak value. The experimental data are plotted as circles. **d**, Amplitude spectra of the time-domain data shown in **c**. **e**, Calculated scaling of the spectral amplitude of the long-lived offset, $A_{0\,\mathrm{THz}}$, for no misalignment (red circles) and a misalignment angle of the near-infrared $\boldsymbol{k}$ vector out of the y–z plane of 1.25° (red spheres). In the spin-switching regime ($E_{\mathrm{THz}} \geq 0.75$ MV cm^{-1}; grey-shaded area), the calculations reproduce the increased slope of $A_{0\,\mathrm{THz}}$ observed in the experiment (Fig. 2d). Dashed lines, guides to the eye.

THz electric field component, whereas the q-afm magnon can only be launched by Zeeman coupling to the THz magnetic field[26], which is not enhanced in the feed gap.

The amplitude of the q-fm magnon is remarkably high, given that the field enhancement is spatially confined to the evanescent near-field region (depth, approximately 13 μm) whereas the magneto-optical signal in the antenna-free case (Fig. 1c, black curve) originates from the entire thickness (60 μm) of the TmFeO$_3$ substrate. A rough estimate (see Methods) shows that the spins in the antenna gap need to undergo a rotation by as much as 24° in order to explain the observed signal strength. Hence, a further increase of the incident THz field may be able to cause complete spin switching.

Figure 2a shows the ultrafast polarization rotation probed in the feed gap, for various far-field THz amplitudes between $E_{\mathrm{THz}} = 0.15$ MV cm^{-1} and 1.0 MV cm^{-1}. For the lowest field, the spin dynamics resemble the q-fm precession sampled in the unstructured crystal (Fig. 1c, black curve). For increasing fields, the oscillation amplitude grows. When the incident THz field exceeds $E_{\mathrm{THz}} = 0.75$ MV cm^{-1}, a qualitatively new behaviour emerges. The period of the first full cycle of the magnetization oscillation is distinctly stretched (see vertical dashed line in Fig. 2a) while a pronounced beating feature occurs in the coherent polarization rotation signal, seen during 25 ps < t < 35 ps. Simultaneously, a long-lived offset of the Faraday signal develops (Fig. 2b, red-shaded area). In the frequency

domain (Fig. 2c), these novel dynamics are associated with an asymmetric splitting of the q-fm magnon resonance superimposed on a broad spectral distribution, somewhat reminiscent of the spectral fingerprint of carrier-wave Rabi oscillations[30]. The long-lived offset (Fig. 2b) manifests itself in a d.c. spectral component, $A_{0\,\mathrm{THz}}$, which grows more rapidly for $E_{\mathrm{THz}} > 0.75$ MV cm^{-1} (Fig. 2d and Extended Data Fig. 2). We will show next that the stretching of the first oscillation cycle, the beating of the Faraday signal and the spectral splitting of the magnon resonance are hallmarks of all-coherent non-perturbative spin trajectories between adjacent minima of the magnetic potential energy, whereas the long-lived offset directly reads out the switched spin state.

The dynamics can best be understood by starting out with the magnetic structure of TmFeO$_3$ (Fig. 3a). The slight canting between the magnetizations $\boldsymbol{M}_1$ and $\boldsymbol{M}_2$ of the two antiferromagnetic sublattices causes a weak ferromagnetic moment $\boldsymbol{F} = \boldsymbol{M}_1 + \boldsymbol{M}_2$ in the x–z plane. The antiferromagnetic vector $\boldsymbol{G} = \boldsymbol{M}_1 - \boldsymbol{M}_2$ encloses an angle ϕ with the x axis. In the Γ_{24} transition phase ($T_1 < T < T_2$), ϕ shifts continuously between 0° and 90° as the magnetic potential $W(\phi)$ changes with the thermal population of the Tm^{3+} crystal-field-split states[26]. $W(\phi)$ features four intrinsically degenerate minima. To ensure that the pump–probe experiment starts with the same equilibrium spin orientation angle ϕ_0 for every laser shot, we apply a weak external magnetic field $B_{\mathrm{ext}} = 100$ mT (see Methods).
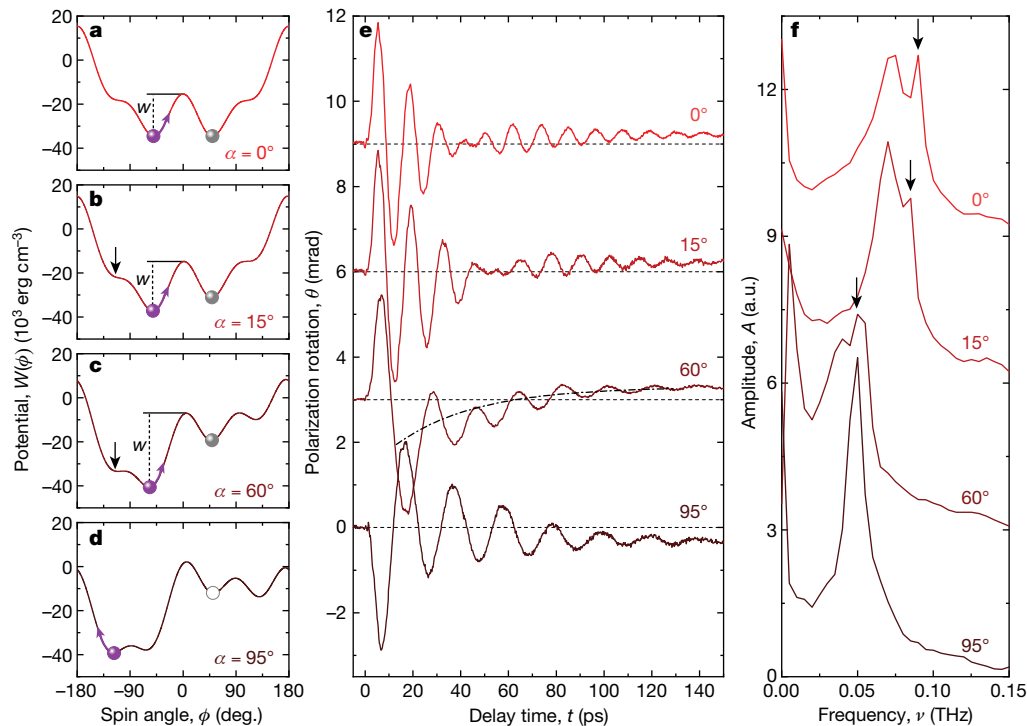
Fig. 4 | Ballistic steering of spins. a–d, Magnetic potential $W(\phi)$ for a lattice temperature of $T = 82.5$ K and various orientations α of the static external magnetic bias, $\boldsymbol{B}_{ext}$. w, potential barrier height relevant for switching; black arrows, potential shoulder associated with the redshift. Violet spheres and arrows, initial spin orientation and direction after excitation; grey spheres, final orientation of switched spins; grey circle,

target spin orientation (not reached). **e,** Polarization rotation as a function of the delay time, t, for the potentials shown in **a–d** and a THz peak far-field amplitude of $E_{THz} = 1.0$ MV cm^{-1}. Dashed-dotted curve, transient negative polarization rotation (see text). Dashed lines, baselines. **f,** Amplitude spectra of the time-domain data shown in **e**. The black arrows mark the computed centre frequencies.

When the intense THz near field excites the Tm^{3+} ions, it abruptly modifies $W(\phi)$, shifting both the position, ϕ_0, and the depth of the potential minimum (Fig. 3b inset). These non-adiabatic changes give rise to a displacive and an impulsive anisotropy torque, which initiate coherent magnetization dynamics as described by the generalized sine-Gordon equation (see Methods). Figure 3b illustrates two typical spin trajectories. For a peak near field of $E_{NF} = 6$ MV cm^{-1}, the spins carry out a coherent oscillation about ϕ_0. A field of $E_{NF} = 10$ MV cm^{-1}, by contrast, allows the spins to overcome the potential barrier at $t = 3.4$ ps, and relax into a new equilibrium position ϕ_1, corresponding to a spin rotation by about 90°. While crossing the potential maximum the spins acquire a characteristic phase, which causes a retardation by approximately 180° with respect to spin oscillations in the initial potential minimum, seen at $t = 9.7$ ps (Fig. 3b, red solid line). Once the spins have reached their maximum positive deflection they oscillate back, but do not overcome the potential barrier a second time because of damping. They rather stay within the new minimum and, in a strongly anharmonic motion, accumulate more phase retardation such that the red and blue trajectories in Fig. 3b oscillate in phase again, around $t \approx 25$ ps.

To link these dynamics with the measured polarization rotation, we calculate the expected Faraday signal by projecting the ferromagnetic moment $\boldsymbol{F}(\phi)$ onto the wave vector of the near-infrared probe pulse, $\boldsymbol{k}_{NIR}$ (see Fig. 3a). By superimposing the contributions of the two spin trajectories in Fig. 3b, the pronounced beating feature ($t \approx 25$ ps) can be associated with the phase slip occurring during spin switching (see Extended Data Fig. 3). For a quantitative analysis, we combine our calculation of the near field induced by the experimental THz wave with a numerical solution of the local generalized sine-Gordon equation (see Methods). We then weight the locally induced Faraday signal by the intensity distribution of the probe beam and sum all the microscopic contributions from the probed volume. Figure 3c shows the calculated polarization rotations, θ, for $E_{THz} = 0.4$ MV cm^{-1} and 1.0 MV cm^{-1} (for fit parameters, see Methods). All experimental

features are quantitatively reproduced, including the quasi-monochromatic magnon oscillation, for low fields (Fig. 3c, blue curve), as well as the phase retardation of the first magnon oscillation period and the pronounced beating at $t \approx 25$ ps, at large THz fields (Fig. 3c, red curve). Moreover, the model unambiguously connects the asymmetric splitting of the q-fm resonance and the broad low-frequency components (Fig. 3d) to THz-driven all-coherent spin switching.

The calculation also confirms that the switched spins can be directly read out. As seen in Fig. 2d, increasing E_{THz} leads to a long-lived signal offset. This is caused by two distinct mechanisms: (i) THz excitation of Tm^{3+} ions slightly shifts the position of the potential minimum (Fig. 3b inset); and (ii) a transfer of spins over the barrier can also change the net magneto-optical signal if $\boldsymbol{k}_{NIR}$ is tilted out of the y–z plane (Fig. 3a). Assuming a tilt angle of 1.25°, we can fit all measured transients in the time domain (Fig. 2). For the corresponding fit parameters, $A_{0\,THz}$ traces the experimental field scaling (Fig. 2d), including the slow increase below the switching threshold, $E_{THz} > 0.75$ MV cm^{-1}, and the steep slope above (Fig. 3e, red spheres). By contrast, a calculation with identical fit parameters but a tilt angle of 0° yields a slow increase of $A_{0\,THz}$ for all field strengths (Fig. 3e, red circles). From this comparison we assign the slow increase to the shift of the potential minimum, whereas the steep slope observed for finite tilt angles can be directly related to the spin transfer over the barrier.

On the basis of the microscopic understanding of the spin dynamics, we can shape the spin trajectory by tailoring the magnetic potential. As a first control parameter (see Extended Data Fig. 4), we lower the temperature to $T = 82.5$ K, at which the barrier height, w, is slightly increased (Fig. 4a). Consequently, the switching dynamics are decelerated and the beating signature is delayed to $t = 45$ ps (Fig. 4e, top curve). Meanwhile, the spectrum remains qualitatively similar (Fig. 4f, top curve). The barrier height can also be raised by rotating the external magnetic bias field, $\boldsymbol{B}_{ext}$, by an angle $\alpha = 15°$ about the optical axis (Fig. 4b and Extended Data Fig. 1), resulting in a shift of the beating feature to a delay of $t = 55$ ps (Fig. 4e). Thereby, the potential shoulder

at $\phi = -115°$ is lowered (Fig. 4b), which enables large-amplitude oscillations throughout a slightly wider potential trough, causing a weak redshift of the spectrum (Fig. 4f). For $\alpha = 60°$ (Fig. 4c), the dynamics are strongly altered (Fig. 4e, f). After the spins are driven up the potential barrier at $\phi = 0°$ during the first half cycle, the non-switching spins oscillate back through the wide potential minimum that is extended by the shoulder at $\phi = -115°$. This results in a strong redshift of the centre frequency to 50 GHz. On the potential shoulder, the projection $\boldsymbol{F} \cdot \boldsymbol{k}_{NIR}$ drops below its initial value at ϕ_0 (Extended Data Fig. 5), leading to a transient negative offset of the Faraday signal (Fig. 4e, dashed-dotted line, and Extended Data Fig. 6) until the oscillations of the unswitched spins have decayed within the starting local potential minimum. A sufficiently large fraction of spins still reach the target valley (grey sphere) for beating to be observed. Finally, $\alpha = 95°$ sets a new starting position and direction of acceleration (Fig. 4d, violet sphere and arrow), causing a reversal of the transient polarization rotation signal and offset (Fig. 4e and Extended Data Fig. 5). The wide potential minimum leads to a reduced centre frequency reproduced by calculating the single spin dynamics (Fig. 4f, black arrows). The large barrier to the neighbouring valley (Fig. 4d, grey circle) inhibits switching completely and no beating is observed.

The unprecedented phase slip, the asymmetric spectral splitting, and the long-lived offset in the magneto-optical response occurring above a well-defined threshold peak field are the fingerprints of ballistic spin switching, marking a novel regime of ultrafast all-coherent spin control throughout the entire phase space. In our specific implementation of a THz-driven anisotropy torque, the absorption of approximately one THz photon energy per spin suffices for switching while the energy dissipation within the spin system remains below 1 μeV per spin (see Methods). This scheme is, thus, highly scalable. Future storage devices could exploit the excellent spatial definition of antenna structures (Extended Data Fig. 7) to switch magnetic bits of 10 nm diameter with THz energies of less than 1 attojoule. Owing to the absence of magnetic stray fields, these cells could be densely packed, similar to vortex core structures in ferromagnetic thin films[14]. The readout of the spin state could be combined with spintronic approaches[20,24]. Such optimized antennas with nanoscale gaps providing field enhancement factors of 10^4 and more could be driven by all-electronic on-chip THz sources, enabling practical implementations of novel spin memories operating at THz clock rates and with the lowest possible dissipation.

Online content

Any methods, additional references, Nature Research reporting summaries, source data, statements of data availability and associated accession codes are available at https://doi.org/10.1038/s41586-019-1174-7.

1. Wang, Y. H., Steinberg, H., Jarillo-Herrero, P. & Gedik, N. Observation of Floquet–Bloch states on the surface of a topological insulator. *Science* **342**, 453–457 (2013).
2. Matsunaga, R. et al. Light-induced collective pseudospin precession resonating with Higgs mode in a superconductor. *Science* **345**, 1145–1149 (2014).
3. Mitrano, M. et al. Possible light-induced superconductivity in K_3C_{60} at high temperature. *Nature* **530**, 461–464 (2016).
4. Hohenleutner, M. et al. Real-time observation of interfering crystal electrons in high-harmonic generation. *Nature* **523**, 572–575 (2015).
5. Garg, M. et al. Multi-petahertz electronic metrology. *Nature* **538**, 359–363 (2016).
6. Sivis, M. et al. Tailored semiconductors for high-harmonic optoelectronics. *Science* **357**, 303–306 (2017).
7. Higuchi, T., Heide, C., Ullmann, K., Weber, H. B. & Hommelhoff, P. Light-field-driven currents in graphene. *Nature* **550**, 224–228 (2017).
8. Langer, F. et al. Lightwave valleytronics in a monolayer of tungsten diselenide. *Nature* **557**, 76–80 (2018).
9. Back, C. H. et al. Minimum field strength in precessional magnetization reversal. *Science* **285**, 864–867 (1999).
10. Tudosa, I. et al. The ultimate speed of magnetic switching in granular recording media. *Nature* **428**, 831–833 (2004).
11. Kim, T. H., Grünberg, P., Han, S. H. & Cho, B. K. Precessional switching of antiferromagnets by electric field induced Dzyaloshinskii-Moriya torque. *Phys. Rev. B* **97**, 184427 (2018).
12. Landauer, R. Irreversibility and heat generation in the computing process. *IBM J. Res. Develop.* **5**, 183–191 (1961).
13. Madami, M., Chiuchiù, D., Carlotti, G. & Gammaitoni, L. Fundamental energy limits in the physics of nanomagnetic binary switches. *Nano Energy* **15**, 313–320 (2015).
14. Van Waeyenberge, B. et al. Magnetic vortex core reversal by excitation with short bursts of an alternating field. *Nature* **444**, 461–464 (2006).
15. Kimel, A. V., Kirilyuk, A., Tsvetkov, A., Pisarev, R. V. & Rasing, T. Laser-induced ultrafast spin reorientation in the antiferromagnet $TmFeO_3$. *Nature* **429**, 850–853 (2004).
16. Kimel, A. V. et al. Inertia-driven spin switching in antiferromagnets. *Nat. Phys.* **5**, 727–731 (2009).
17. Li, T. et al. Femtosecond switching of magnetism via strongly correlated spin–charge quantum excitations. *Nature* **496**, 69–73 (2013).
18. Beaurepaire, E., Merle, J.-C., Daunois, A. & Bigot, J.-Y. Ultrafast spin dynamics in ferromagnetic nickel. *Phys. Rev. Lett.* **76**, 4250–4253 (1996).
19. Stupakiewicz, A., Szerenos, K., Afanasiev, D., Kirilyuk, A. & Kimel, A. V. Ultrafast nonthermal photo-magnetic recording in a transparent medium. *Nature* **542**, 71–74 (2017).
20. Jungwirth, T., Marti, X., Wadley, P. & Wunderlich, J. Antiferromagnetic spintronics. *Nat. Nanotechnol.* **11**, 231–241 (2016).
21. Kampfrath, T. et al. Coherent terahertz control of antiferromagnetic spin waves. *Nat. Photon.* **5**, 31–34 (2011).
22. Nova, T. F. et al. An effective magnetic field from optically driven phonons. *Nat. Phys.* **13**, 132–136 (2017).
23. Lu, J. et al. Coherent two-dimensional terahertz magnetic resonance spectroscopy of collective spin waves. *Phys. Rev. Lett.* **118**, 207204 (2017).
24. Olejník, K. et al. Terahertz electrical writing speed in an antiferromagnetic memory. *Sci. Adv.* **4**, eaar3566 (2018).
25. Kubacka, T. et al. Large-amplitude spin dynamics driven by a THz pulse in resonance with an electromagnon. *Science* **343**, 1333–1336 (2014).
26. Baierl, S. et al. Nonlinear spin control by terahertz-driven anisotropy fields. *Nat. Photon.* **10**, 715–718 (2016).
27. Liu, M. et al. Terahertz-field-induced insulator-to-metal transition in vanadium dioxide metamaterial. *Nature* **487**, 345–348 (2012).
28. Lange, C. et al. Extremely nonperturbative nonlinearities in GaAs driven by atomically strong terahertz fields in gold metamaterials. *Phys. Rev. Lett.* **113**, 227401 (2014).
29. Staub, U. et al. Interplay of Fe and Tm moments through the spin-reorientation transition in $TmFeO_3$. *Phys. Rev. B* **96**, 174408 (2017).
30. Mücke, O. D., Tritschler, T., Wegener, M., Morgner, U. & Kärtner, F. X. Signatures of carrier-wave Rabi flopping in GaAs. *Phys. Rev. Lett.* **87**, 057401 (2001).

Author contributions S.S., C.L., S.B. and R.H. designed and implemented the antenna structures. R.V.M. and A.V.K. identified the bulk material for the project. S.S., C.L., S.B., T.E., C.P.S. and D.C.V. carried out the experiment with support from R.V.M. The theoretical modelling was carried out by C.L., S.S., S.B., A.K.Z. and R.V.M. A.V.K. and R.H. supervised the study. All authors analysed the data, discussed the results and contributed to the writing of the manuscript.

METHODS

Sample preparation. We used a monocrystalline, 60-μm-thick TmFeO₃ sample obtained by floating-zone melting. The sample was cut perpendicularly to one of the crystal's optical axes, which lies in the y–z plane at an angle of 51° with respect to the z axis. The custom-tailored THz antennas with a feed gap of 3.5 μm and a resonance frequency of 0.65 THz were processed on top of the crystal by electron-beam lithography of a poly(α-methylstyrene-co-α-chloracrylate methylester) resist, subsequent evaporation of 100 nm of gold, and lift-off. The structure was kept in a helium cryostat and cooled to temperatures within the Γ_{24} transition phase. For the measurements discussed in the first part of the manuscript, a static bias field of $B_{ext} = 100$ mT from a permanent magnet was applied within the y–z plane of the crystal at an angle of 39° relative to the z axis, defining the equilibrium spin orientation ϕ_0 and ensuring the restoring of the magnetization between subsequent laser pulses. For the data shown in Fig. 4, the B field was rotated about the optical axis of the crystal, whereby an angle of $\alpha = 0°$ denotes the starting position within the y–z plane as defined above.

Experimental set-up. Intense single-cycle THz pulses were generated by tilted-pulse front optical rectification of near-infrared pulses from a low-noise Ti:sapphire laser amplifier (centre wavelength, 807 nm; pulse energy, 5.5 mJ; pulse duration, 33 fs; repetition rate, 3 kHz) in a cryogenically cooled LiNbO₃ crystal (Extended Data Fig. 1b). A pair of wire-grid polarizers were used to control the peak field strength and the polarization state of the THz waveforms. Extended Data Fig. 1c, d shows the THz transient and the corresponding spectrum featuring frequency components between 0.3 and 2.5 THz. A small portion of the near-infrared power was sent through a delay line, combined with the THz pulse using a fused silica window coated with indium tin oxide, and collinearly transmitted through the feed gap of the antenna structure to probe the magnetization state. The polarization rotation was measured by subsequent optics consisting of a half-wave plate, a Wollaston prism, and two balanced silicon photodiodes, read out by a lock-in amplifier. In order to calibrate the THz field amplitude in the sample focus, the focal diameter was determined by measuring the THz power transmitted through a circular aperture. The corresponding total energy was then calculated by time-integration of $E_{THz}(t)$ (ref. [2]). We estimate that the total uncertainty of the field amplitude amounts to 16%.

Estimate of the spin switching energy. The Poynting theorem dictates that the absorbed electro-magnetic power density $P(t)$ is given by

$$P(t) = j(t)E(t) \tag{1}$$

where $j(t)$ is the effective current density describing dissipative processes in a material and $E(t)$ is the oscillating electric field. The full energy absorbed per unit volume is therefore:

$$W_{abs} = \int_{-\infty}^{\infty} j(t)E(t)\,dt \tag{2}$$

By taking the Fourier transforms $j(t) = \frac{1}{2\pi}\int_{-\infty}^{\infty}\tilde{j}(\omega)e^{i\omega t}d\omega$ and $E(t) = \frac{1}{2\pi}\int_{-\infty}^{\infty}\tilde{E}(\omega')e^{iw't}d\omega'$, where ω is the frequency, and $\tilde{j}(\omega)$ and $\tilde{E}(\omega)$ are the Fourier transformations of $j(t)$ and $E(t)$, respectively. Substituting them into equation (2) we obtain:

$$W_{abs} = \frac{1}{2\pi}\int_{-\infty}^{\infty}\tilde{j}(\omega)\tilde{E}(-\omega)d\omega \tag{3}$$

The current density is connected to the electric field by the effective conductivity $\sigma(\omega) = \frac{\tilde{j}(\omega)}{\tilde{E}(\omega)}$, leading to:

$$W_{abs} = \frac{1}{2\pi}\int_{-\infty}^{\infty}\sigma(\omega)\tilde{E}(\omega)\tilde{E}(-\omega)d\omega = \frac{1}{2\pi}\int_{-\infty}^{\infty}\sigma(\omega)|\tilde{E}(\omega)|^2\,d\omega \tag{4}$$

In the case of crystal-field-split ground-state transitions of TmFeO₃ in the temperature interval between 80 K and 90 K, where the imaginary part of the dielectric function ε_2 is much smaller than its real part ε_1 (see ref. [31]), the effective conductivity can be approximated by $\sigma = \varepsilon_0 n_{sub} c\, \alpha_{eff}$. Here $n_{sub} = 4.92$ is the refractive index of TmFeO₃, and $\alpha_{eff} \approx 4{,}000$ m^{-1} is the effective THz absorption coefficient obtained from data of ref. [31], taking into account the spectral shape of our THz pulse. We obtain

$$W_{abs} = \frac{1}{2\pi}\varepsilon_0 n_{sub} c\, \alpha_{eff}\int_{-\infty}^{\infty}|\tilde{E}(\omega)|^2\,d\omega \tag{5}$$

which can be rewritten in the time domain (compare equations (2) and (3)) as:

$$W_{abs} = \varepsilon_0 n_{sub} c\, \alpha_{eff}\int_{-\infty}^{\infty}E^2(t)\,dt \tag{6}$$

The absorbed energy density in the rare-earth system for a near-field THz transient with a peak electric field of 7.8 MV cm^{-1}, which exceeds the threshold for spin switching, is $W_{abs} = 20$ J cm^{-3}. TmFeO₃ crystallizes in a distorted perovskite structure with a unit cell volume of $V_{uc} = 2.22 \times 10^{-28}$ m^3 (lattice constants: $a = 525$ pm, $b = 557$ pm and $c = 758$ pm) (see ref. [32]), which contains 4 Fe^{3+} spins. Thus, an upper bound for the absorbed energy in the rare-earth system per spin is given by $W_{spin} = W_{abs} \times \frac{V_{uc}}{4} = 7.15$ meV, which is of the order of the energy of one THz photon. The dissipation by the spin system is even smaller: the energy required to overcome the potential barrier that separates two neighbouring potential minima (see Fig. 3b), normalized by the number of spins in the switched volume, is less than 1 μeV. This value can, thus, be regarded as an upper limit for the maximal energy dissipated by one spin upon switching.

Estimate of the magnetization deflection in the near-field volume. In the case of unstructured bulk TmFeO₃, the total polarization rotation, θ, results from approximately equal contributions across the entire sample thickness of 60 μm. In order to calibrate the relation between θ and the spin angle ϕ, we enforce a full switching of the magnetization (change of ϕ by 180°) by reversing the external static magnetic bias field. This scenario rotates the probe polarization by 24 mrad. Thus, we conclude that a polarization rotation of $\theta = 0.5$ mrad, as induced by a THz amplitude of 1.0 MV cm^{-1} in the antenna-free sample, corresponds to a transient spin excursion of $\Delta\phi = 3.5°$. Taking into account the quadratic dependence of $\Delta\phi$ on the electric field amplitude[26], we link the polarization rotation to the THz peak electric field by $\theta = \xi L \bar{E}_{peak}^2$, where L is the crystal length, $\xi = 472$ mrad cm (MV)$^{-2}$ is the coupling constant, and $\bar{E}_{peak} = 0.42$ MV cm^{-1} is the peak electric THz amplitude averaged over the length of the unstructured TmFeO₃ sample. In the antenna-covered structure, the magneto-optical signal can be divided into two contributions: the antenna near-field region extending down to a depth of 13 μm below the antenna (Extended Data Fig. 8, red-shaded area), where electric fields strongly exceeding the far-field amplitude are encountered, and a bulk part (Extended Data Fig. 8, blue-shaded area), where the electric field assumes an average value of 0.3 MV cm^{-1}. Accordingly, the polarization rotation by the bulk part is $\theta_b = \xi \times (47\,\mu m) \times (0.3\text{ MV cm}^{-1})^2 = 0.2$ mrad, such that 0.7 mrad of the total magneto-optical signal result from the near-field volume. This contribution corresponds to an average spin deflection angle of $\Delta\phi = 24°$.

Numerical calculation of antenna response. The THz response of the entire structure, including the near field of the custom-tailored antenna as well as the substrate, was obtained by solving Maxwell's equations using a finite-difference frequency-domain (FDFD) approach. The refractive index of TmFeO₃ is set to $n_{sub} = 4.92$, while the gold structure is implemented as a perfect metal. The THz near-field waveforms were subsequently calculated on the basis of the measured far-field THz waveform, employing the results of the FDFD calculations as a complex-valued transfer function. These near-field waveforms enabled us to retrieve the local dynamics of the spin deflection angle, ϕ, by time-domain numerical integration as detailed below. The overall polarization rotation was obtained by integrating the local contributions along the entire probe volume, weighted by the intensity profile of the probe beam. We used a diameter of 6 μm (FWHM) in the direction parallel to the capacitor plates, and 2 μm (FWHM) in the orthogonal direction in order to account for diffraction effects near the capacitive plates. While calibrating near fields in excess of about 10 MV cm^{-1} is challenging[27,28], the total polarization rotation is robust against variations of the maximum near fields occurring only in the close vicinity of the capacitive plates, as confirmed by calculations. A grid resolution of $(100\text{ nm})^3$ was chosen for proper convergence.

Calculation of spin dynamics. We adapted the previously derived formalism for THz-induced spin dynamics based on the generalized sine-Gordon equation for our high-field setting[26]. The vectorial spin orientation can be mapped onto the angle ϕ between the antiferromagnetic vector G and the x axis (Fig. 3a). The magnetic potential $W(\phi)$ of TmFeO₃ is given by[26]

$$W(\phi) = K_1\sin^2\phi + K_2\sin^4\phi$$
$$- \frac{H_D}{H_E}M_{Fe} \times (B_{ext}\cos\alpha\,\cos\phi - B_{ext}\sin\alpha\,\sin\phi - B_{THz}\sin\phi) \tag{7}$$

where $H_D = 2 \times 10^5$ Oe is the Dzyaloshinskii field, $H_E = 2 \times 10^7$ Oe is the effective field of the d–d exchange, and $M_{Fe} = 1{,}000$ e.m.u. cm^{-3} is the magnetization of a single Fe^{3+} sublattice[33]. The parameter $K_1 = 2K_2\frac{T - T_2}{T_2 - T_1}$ for $T_1 < T < T_2$, where K_2 is a constant, sets the potential curvature by the frequency of the quasi-ferromagnetic mode $\omega_{q-fm}^2 = \frac{1}{2}\omega_E\omega_A\sin^2\phi_0$ in the linear regime of spin dynamics. Here, $\omega_E = \gamma H_E$, $\omega_A = \gamma\frac{K_2}{M_{Fe}}\gamma$ is the gyromagnetic ratio, T is the spin lattice temperature,

and $T_1 = 80$ K and $T_2 = 90$ K are the lower and upper temperature bounds of the Γ_{24} transition phase, respectively. The thermal excitations of the crystal-field-split ground states determine the equilibrium angle of the spin vector, $\phi_0 = \arcsin\left(\frac{T - T_2}{T_2 - T_1}\right)^{\frac{1}{2}}$ (see ref. [26]). For our numerical simulations, we calibrated the effective magnetic potential $W(\phi)$ by the experiment with bulk TmFeO$_3$, and we included an external magnetic field along the z axis ($\alpha = 0$) of $B_{ext} = 150$ mT compatible with the experimentally determined value. As we are operating in the high-field regime, where the THz-induced nonlinear anisotropy torque dominates[26], we neglect the magnetic THz spin interaction with the THz magnetic field, B_{THz}, which is oriented along the crystallographic x axis.

The equation of motion accounting for a THz-induced change of the magnetic potential energy reads:

$$\ddot{\phi} - C^2 \nabla^2 \phi = -\gamma_D \dot{\phi} + \omega_E \omega_A \cos(\phi)\sin(\phi) \times (\eta + \sin^2(\phi))$$
$$+ \kappa \cos(\phi)\sin(\phi)\varepsilon_0 n_{sub} c\, \alpha_{eff} E_{THz}^2 - \frac{H_D}{H_E}\gamma\, \omega_E B_{ext}\sin\phi \quad (8)$$

Here, γ_D is the damping. The excitation by the crystal field transitions is modelled by both an impulsive and a displacive mechanism, accounting for an increase of the angular velocity, $\dot{\phi}$, and a shift of the equilibrium spin angle, ϕ_0, respectively, in conceptual analogy to ref. [34]. The impulsive excitation is implemented by the term proportional to the constant κ, coupling the spin dynamics to the instantaneous THz power density $\varepsilon_0 n_{sub} c \alpha_{eff} E_{THz}^2$. To account for the displacive term, we implement a strong THz-induced excitation of the crystal field transitions, leading to an increase of the population density $\Delta\rho(t)$ of the excited states of the Tm^{3+} ions. In our model, this is described by the excitation parameter $\eta = \frac{(\rho(T) + \Delta\rho(t)) - \rho_2}{\rho_2 - \rho_1}$, where $\rho(T)$, ρ_1 and ρ_2 are the equilibrium population densities of the crystal-field-split states at temperatures T, T_1 and T_2, respectively. The THz-induced change of the population density leads to an abrupt change of the magnetic potential, $W(\phi)$, of the iron spins, resulting in a displacive anisotropy torque. Quantitatively, we calculate $\Delta\rho(t) = \Gamma \int_{-\infty}^{t} \frac{\varepsilon_0 n_{sub} c\, \alpha_{eff}}{\hbar \omega_{CFT}} E_{THz}^2(t') \mathrm{d}t'$, where Γ is a coupling parameter, $\hbar$ is the reduced Planck's constant, and ω_{CFT} is the resonance frequency of the electric dipole active Tm^{3+} ground-state transition[35]. The term $C^2\nabla^2\phi$ accounts for the interaction between different magnetic domains of the sample, where C is the spin wave velocity that sets the maximal speed of a domain boundary. In the orthoferrites[36,37], $C = 2 \times 10^6$ cm s^{-1}. One can see that, on the ~1 ps timescale of our experiment, the regions of the sample exposed to the THz fields of different strengths can be assumed to be practically non-interacting as the magnetic excitations travel a distance of 10 nm during this time. This distance is also much smaller than the characteristic spatial scale of the THz near field of >1 μm. We therefore neglected the term $C^2\nabla^2\phi$ in our numerical simulations.

The local dynamics of the spin deflection angle, ϕ, are calculated by solving equation (8) separately for each near-field cell using the corresponding THz near-field transient (see Supplementary Video 1). As confirmed by polarimetry, the THz-induced change of the magnetization leads to a rotation of the near-infrared probe polarization. A switch-off analysis shows that the Faraday rotation is almost exclusively caused by the ferromagnetic component of the magnetization, while the dynamics of the antiferromagnetic response play a minor part. Thus, the microscopic Faraday rotation is obtained by projecting the ferromagnetic vector, $F(\phi)$, of each cell onto the wave vector of the near-infrared probe beam, k_{NIR}. Integration of these contributions along the optical axis allows us to quantitatively reproduce the experimentally detected polarization rotation, θ (see Fig. 3c). In the non-perturbative regime, the actual spin trajectory depends sensitively on the exact location within the near-field region of the antenna. Yet the total magneto-optical response integrated over the entire near-field volume is fairly robust against minor field fluctuations. For our measurement with a far-field THz peak amplitude of $E_{THz} = 0.4$ MV cm^{-1}, we obtain the best agreement (Fig. 3c, blue curve) using the experimentally determined spin dephasing rate $\gamma_D = 45$ GHz, as well as the following values: $\omega_{q\text{-fm}}/2\pi = 88.7$ GHz, $\kappa = 3.58 \times 10^8$ m^2 W s^{-2} and $\Gamma = 2.49 \times 10^{-10}$ m^3 s. For a THz peak amplitude of $E_{THz} = 1.0$ MV cm^{-1} (Fig. 3c, red curve), we slightly adjust some of the parameters to $\omega_{q\text{-fm}}/2\pi = 90.0$ GHz, $\kappa = 1.02 \times 10^8$ m^2 W s^{-2} and $\Gamma = 1.01 \times 10^{-10}$ m^3 s. Magnon–magnon scattering can effectively be accounted for by introducing a momentum dependent damping in the spin system. Extended Data Fig. 9 shows the results of a switch-off analysis considering three scenarios including the full calculation (solid lines), only the displacive contribution (dashed lines) and only the impulsive contribution (dashed-dotted lines). Whereas for a field amplitude of $E_{THz} = 0.4$ MV cm^{-1}, the sum of displacive and impulsive contributions approximates the full calculation, the strong-field dynamics at $E_{THz} = 1.0$ MV cm^{-1} are only rendered correctly by the full calculation. In all cases, a purely displacive effect yields an exclusively positive magneto-optical signal and a non-zero signal offset, while the impulsive component is responsible for the strong oscillatory component.

Data availability

The data supporting the findings of this study are available from the corresponding authors upon request.

31. Zhang, K. et al. Resolving the spin reorientation and crystal-field transitions in TmFeO$_3$ with terahertz transient. *Sci. Rep.* **6**, 23648 (2016).
32. Leake, J. A., Shirane, G. & Remeika, J. P. The magnetic structure of thulium orthoferrite, TmFeO$_3$. *Solid State Commun.* **6**, 15–17 (1968).
33. Srinivasan, G. & Slavin, A. N. *High Frequency Processes in Magnetic Materials* (World Scientific, Singapore, 1995).
34. Garrett, G. A., Albrecht, T. F., Whitaker, J. F. & Merlin, R. Coherent THz phonons driven by light pulses and the Sb problem: what is the mechanism? *Phys. Rev. Lett.* **77**, 3661 (1996).
35. Kozlov, G. V. et al. Observation of magnetic dipole and electric dipole electron transitions in the ground multiplet of the rare-earth ion in TmFeO$_3$. *JETP Lett.* **52**, 264–268 (1990).
36. Zvezdin, A. K. Dynamics of domain walls in weak ferromagnets. *JETP Lett.* **29**, 553–556 (1979).
37. Chetkin, M. V. & de La Campa, A. Maximum velocity of a domain wall in a weak ferromagnet. *JETP Lett.* **27**, 157–160 (1978).
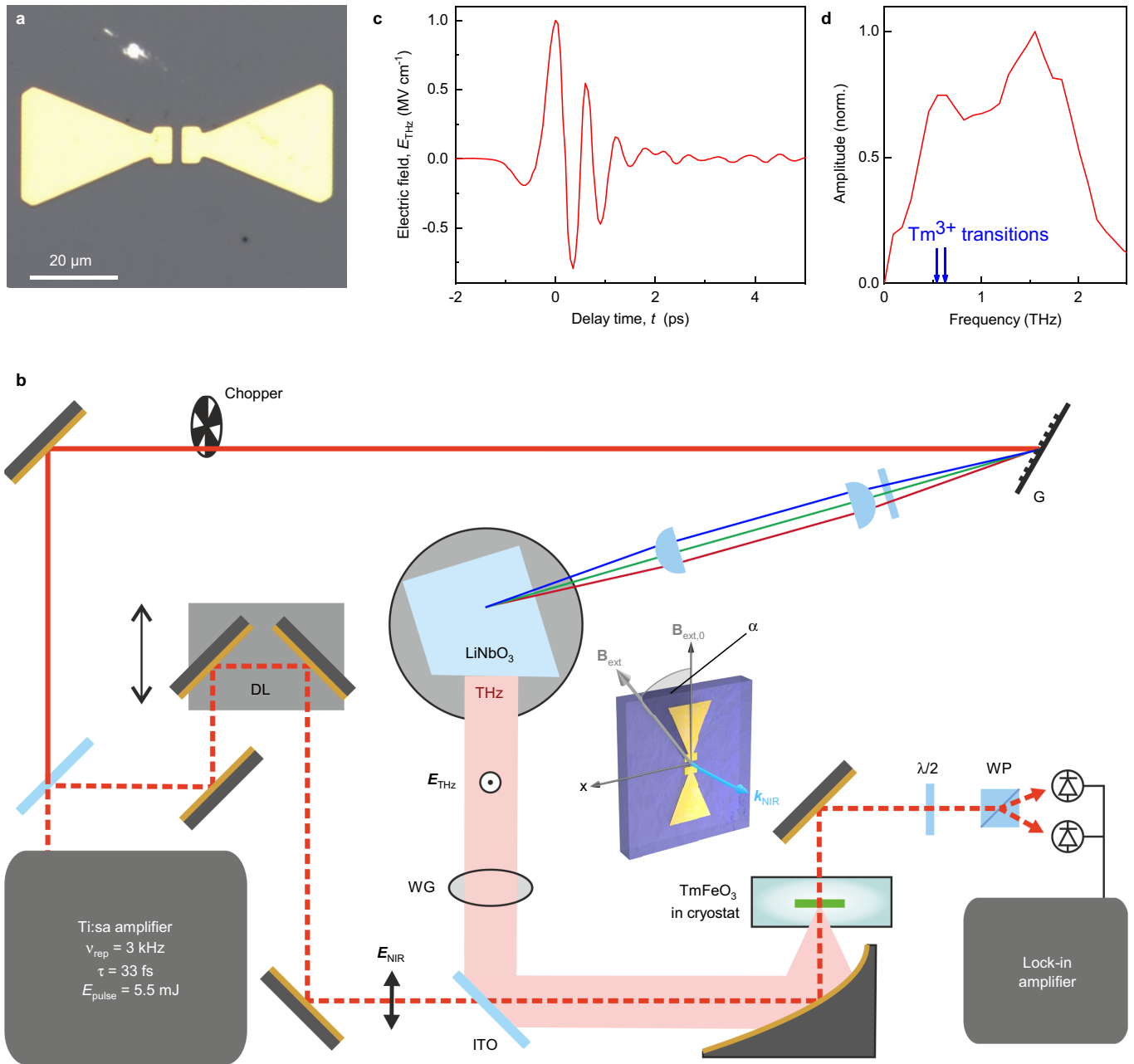
Extended Data Fig. 1 | Experimental set-up. a, Microscope image of the gold bowtie antenna with a resonance frequency of 0.65 THz and a feed gap of 3.5 μm, structured onto the $TmFeO_3$ sample. **b**, Diagram of the experiment. The Ti:sapphire amplifier generates 33-fs light pulses centred at a wavelength of 807 nm, with a pulse energy (E_{pulse}) of 5.5 mJ, and a repetition rate (ν_{rep}) of 3 kHz. The near-infrared beam (red solid line) is dispersed by the grating (G, top right) as visualized by the red, green and blue lines, imprinting a pulse front tilt. Two cylindrical lenses image and focus the laser light into a cryogenically cooled lithium niobate crystal ($LiNbO_3$). WG, pair of wire grid polarizers controlling the intensity and the polarization state of the generated THz pulses. ITO, indium tin oxide coated fused silica window. The THz-induced polarization changes are decoded with the help of a half-wave plate ($\lambda/2$), a Wollaston polarizer (WP) and a pair of photodiodes, and subsequently detected with a lock-in amplifier. DL, mechanical delay line. E_{NIR}, polarization of the near-infrared probe pulse (red dashed line). E_{THz}, polarization of the THz beam (bright red-shaded area). The inset indicates the orientation of the static magnetic field, B_{ext}, as a function of the angle α relative to the orientation $B_{ext,0}$ used for the measurements in the first part of the manuscript. **c**, Electro-optically detected THz field, E_{THz}, generated by tilted-pulse front optical rectification. **d**, Corresponding spectral amplitude of the THz transient shown in **c**. The blue arrows indicate the frequencies of the Tm^{3+} ground-state transitions relevant for our experiment.
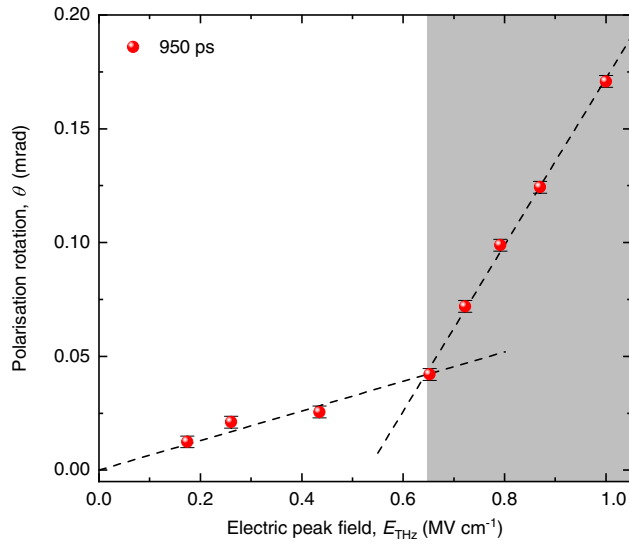
Extended Data Fig. 2 | Scaling of the residual offset for large delay times. Polarization rotation signal at a delay time of $t = 950$ ps as a function of the THz electric peak field, E_{THz}. The data are extracted from time-resolved measurements in the feed gap of an antenna structurally similar to the one discussed in the main text with a feed gap of 3.5 μm and a broad resonance around 0.65 THz, optimized to the Tm^{3+} ground-state transitions. Lattice temperature $T = 81$ K. In the spin switching regime (grey-shaded area), $E_{THz} > 0.65$ MV cm^{-1}, the slope of the polarization rotation signal is substantially increased. Error bars, standard deviation of θ. Dashed lines, guides to the eye.

a

b
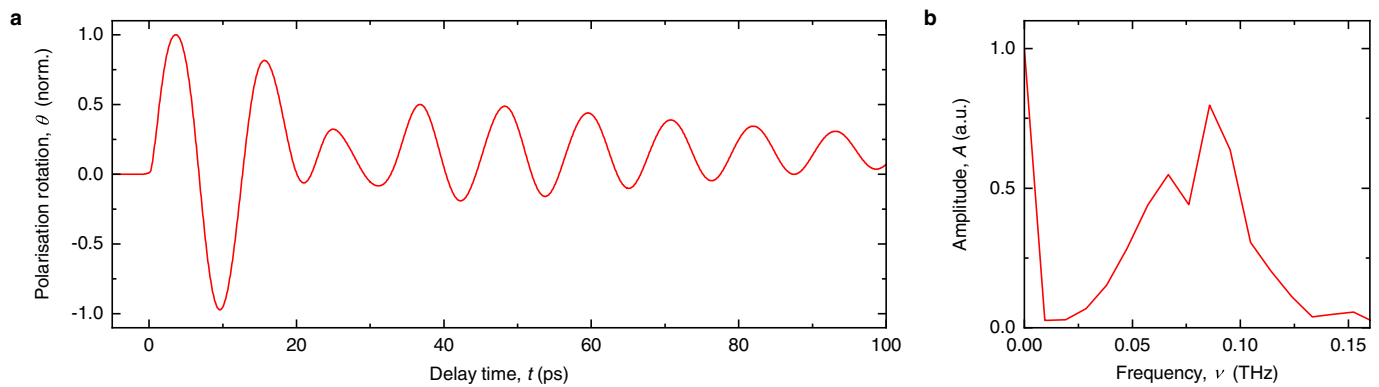
Extended Data Fig. 3 | Qualitative simulation of the beating signature. a, Polarization rotation calculated by superimposing the responses shown in Fig. 3b—that is, spins oscillating in the equilibrium potential minimum at ϕ_0 (relative weight, 0.8) and spins driven into the neighbouring local minimum at ϕ_1 (relative weight, 0.2). **b**, Amplitude spectra of the time-domain data shown in **a**.
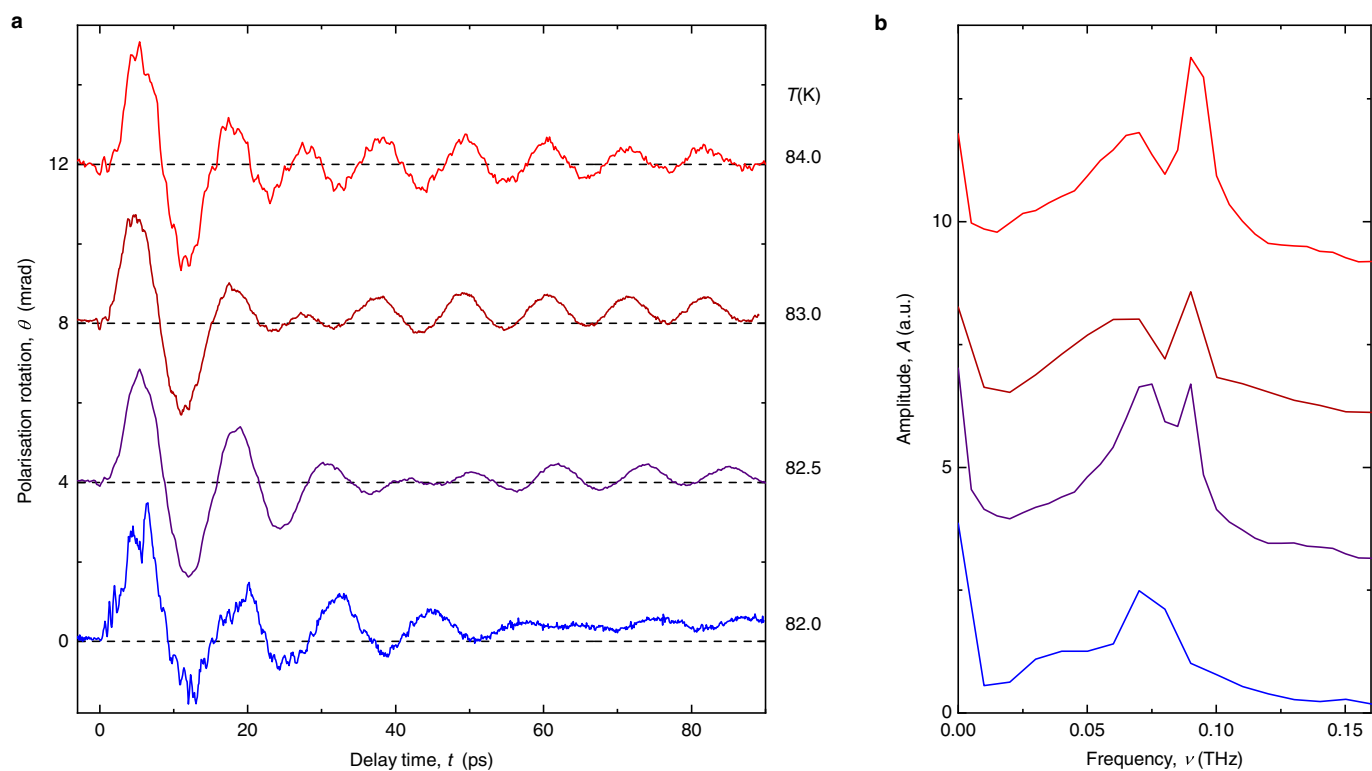
Extended Data Fig. 4 | Temperature dependence of spin dynamics.
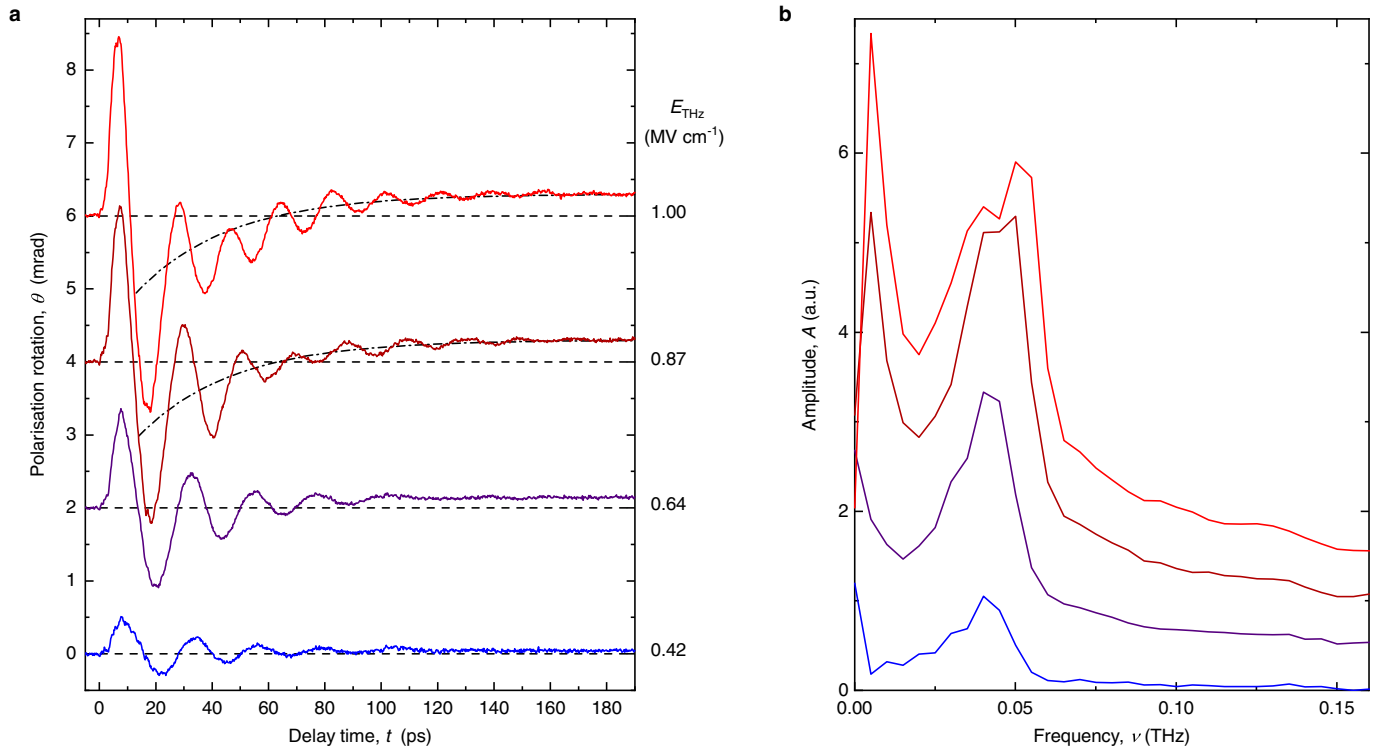**a**, Transient polarization rotation probed in the centre of the feed gap of the antenna discussed in Fig. 4, for a THz far-field amplitude $E_{\mathrm{THz}} = 1.0\ \mathrm{MV\ cm^{-1}}$ and different lattice temperatures, T, between 82.0 K and 84.0 K (shown at right). Dashed lines, baselines. **b**, Corresponding amplitude spectra of the data shown in **a**.
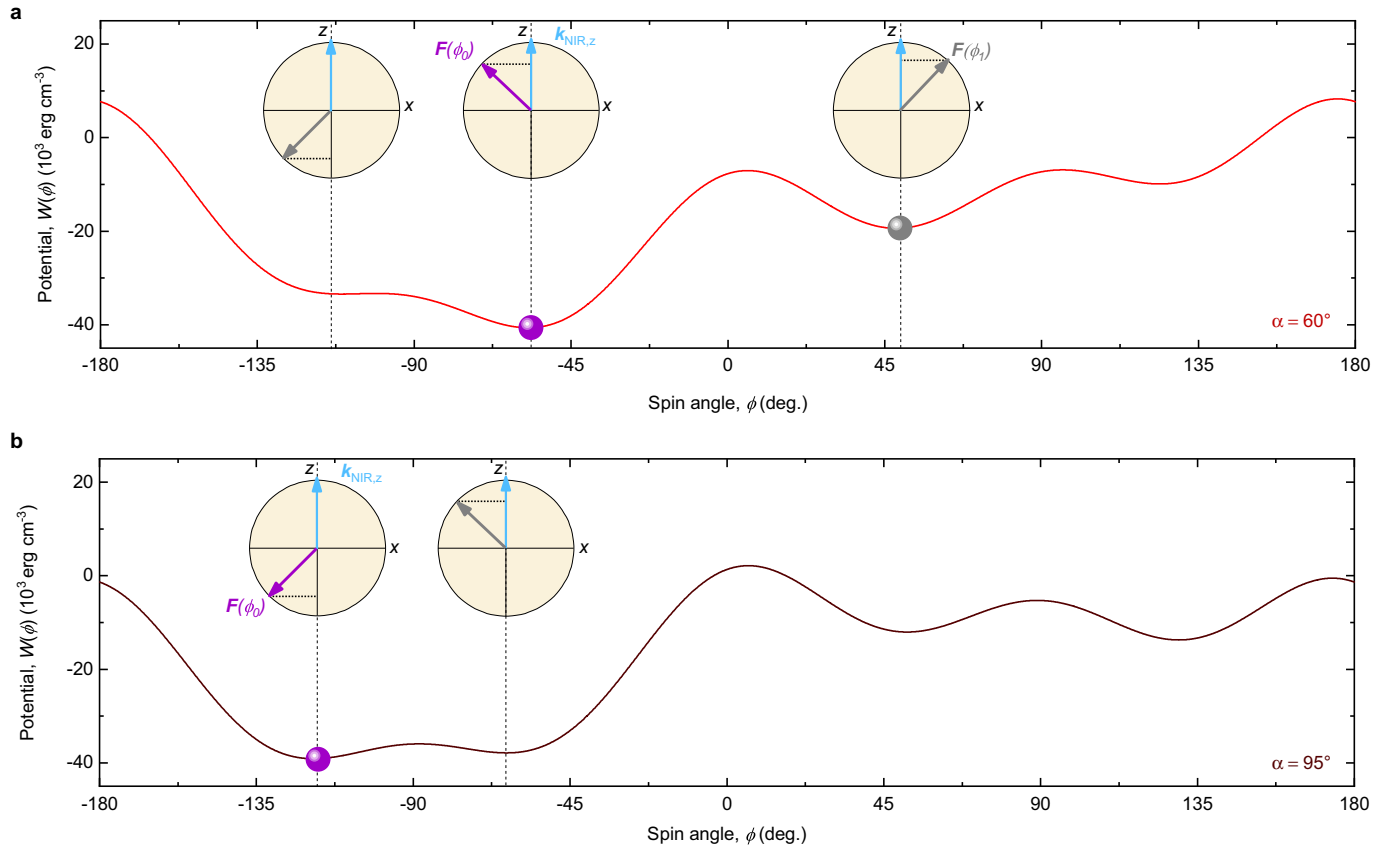
Extended Data Fig. 5 | Faraday signal for spin dynamics in different magnetic potentials. a, Magnetic potential (red curve) for a lattice temperature of $T = 82.5$ K and an angle of B_{ext}, $\alpha = 60°$, as shown in Fig. 4c. Violet (grey) sphere, initial (switched) spin state. Insets, projection (grey dotted horizontal lines) of the magnetization $F(\phi)$ (arrows) onto the near-infrared wave vector, $k_{\text{NIR},z}$ (light blue arrow), for different angles ϕ. For $\phi < \phi_0$, the projection drops below its initial value and becomes negative for $\phi < -90°$, causing a negative transient Faraday signal (Fig. 4e). For $\phi_0 < \phi < \phi_1$, $k_{\text{NIR}} \cdot F(\phi) > k_{\text{NIR}} \cdot F(\phi_0)$, resulting in the positive initial half-cycle of the Faraday rotation signal (Fig. 4e). **b**, Magnetic potential for $\alpha = 95°$ (dark red curve) as shown in Fig. 4d. For $\phi < \phi_0$, the initial spin deflection leads to $k_{\text{NIR}} \cdot F(\phi) < k_{\text{NIR}} \cdot F(\phi_0)$, causing a negative onset of the first oscillation period (Fig. 4e, bottom curve).

Extended Data Fig. 6 | Field dependence of spin dynamics for $\alpha = 60°$.
a, Polarization rotation signal as a function of the delay time, t, for
different THz fields, E_{THz}, between 0.42 MV cm^{-1} and 1.0 MV cm^{-1},
probed in the centre of the feed gap of the antenna discussed in Fig. 4.
The transient negative Faraday signal (dashed-dotted curves) builds up
for $E_{THz} \geq 0.87$ MV cm^{-1}. Dashed lines, baselines. **b**, Corresponding
amplitude spectra of the data shown in **a**.
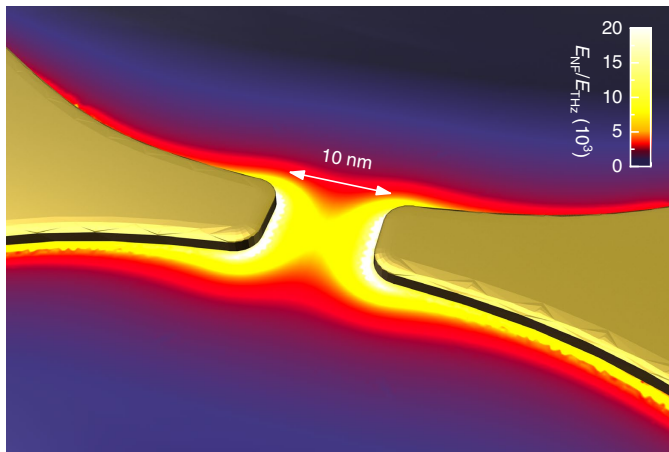
Extended Data Fig. 7 | Electric field enhancement in the near field of a THz nanoantenna. Enhancement factor E_{NF}/E_{THz} (colour scale at right) of the near-field peak amplitude E_{NF} compared to the THz electric far-field E_{THz} calculated by finite-difference simulations for a real THz waveform in the near field of an antenna structure with a feed gap of 10 nm. Assuming a switching threshold of approximately 10 MV cm^{-1}, a far-field amplitude of only 1 kV cm^{-1} is sufficient to drive coherent spin switching by 90° in the centre of the antenna structure.
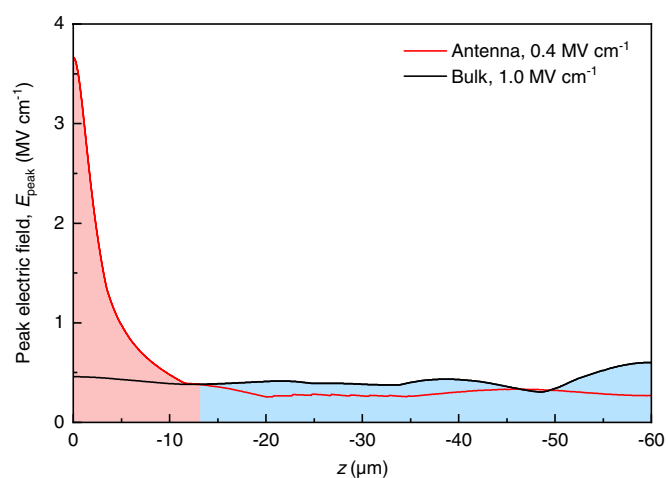
Extended Data Fig. 8 | Calculated electric near-field characteristics of antenna. Near-field amplitude E_{NF} as a function of depth z in the centre of the antenna feed gap, for a THz far-field amplitude of $E_{THz} = 0.4$ MV cm^{-1} ('antenna', red curve). The electric field distribution expected in the unstructured substrate for $E_{THz} = 1.0$ MV cm^{-1} is shown for comparison ('bulk', black line). Red-shaded area, near-field region of the antenna, where the electric field exceeds the value in the bulk structure. Blue-shaded area, bulk part, where the electric field is comparable to the value in the unstructured substrate.
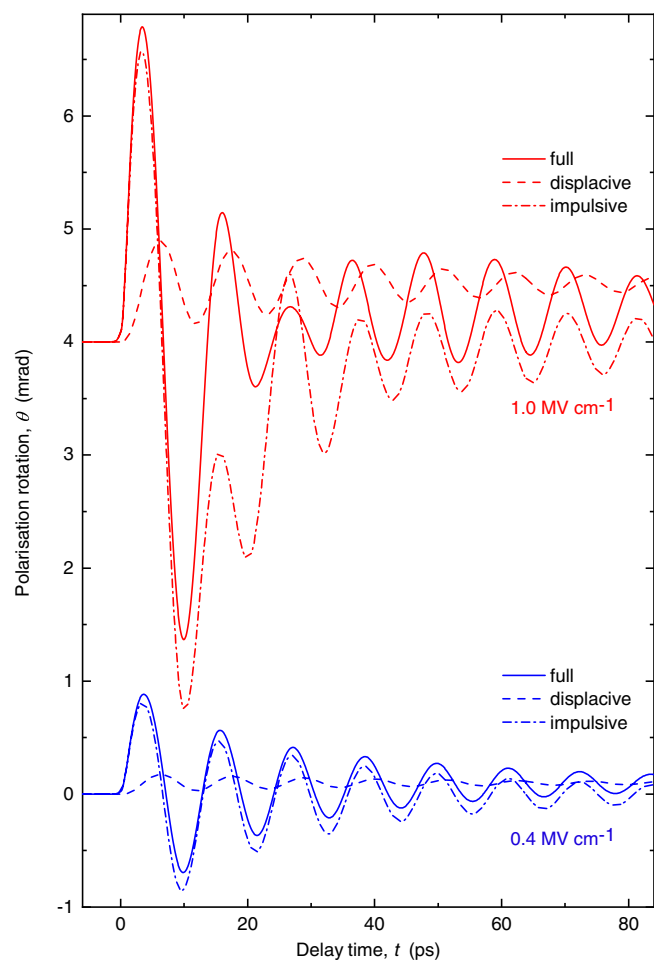
Extended Data Fig. 9 | Simulated magneto-optical response for different driving forces. Calculated polarization rotation signals expected from the antenna structures for a THz far-field amplitude of 0.4 MV cm^{-1} (blue curves) and 1.0 MV cm^{-1} (red curves). Calculations including only the displacive (dashed lines) or impulsive (dashed-dotted lines) anisotropy torque do not fit the experimental data. For the switch-off analysis, the parameters Γ for the displacive and κ for the impulsive torque of the full calculation (solid lines) are used. The curves are offset and normalized to the experimental peak value.